ROM SAF Report 40
Ref: SAF/ROM/DMI/REP/RSR/040
Web: www.romsaf.org
Date: 15 June 2021

EUMETSAT
ROM SAF
RADIO OCCULTATION METEOROLOGY

ROM SAF Report 40

Anomalous GRAS radio occultations

I Culverwell

Met Office

Document Author Table

	Name	Function	Date
Prepared by:	I. D. Culverwell	ROM SAF Project Team	15 June 2021
Reviewed by:	J. R. Eyre	Met Office	26 Feb 2021
Reviewed by:	S. B. Healy	ROM SAF Science Coordinator	15 Jun 2021
Approved by:	K. B. Lauritsen	ROM SAF Project Manager	15 Jun 2021

Document Change Record

Issue/Revision	Date	By	Description
Version 0.1	23 December 2020	IDC	First draft
Version 0.2	24 February 2021	IDC	Second draft
Version 0.3	9 March 2021	IDC	Third draft, incorporating JRE's comments
Version 1.0	15 June 2021	IDC	Final version, incorporating SBH's comments

ROM SAF

The Radio Occultation Meteorology Satellite Application Facility (ROM SAF) is a decentralised processing centre under EUMETSAT which is responsible for operational processing of GRAS radio occultation (RO) data from the Metop and Metop-SG satellites and radio occultation data from other missions. The ROM SAF delivers bending angle, refractivity, temperature, pressure, humidity, and other geophysical variables in near real-time for NWP users, as well as reprocessed Climate Data Records (CDRs) and Interim Climate Data Records (ICDRs) for users requiring a higher degree of homogeneity of the RO data sets. The CDRs and ICDRs are further processed into globally gridded monthly-mean data for use in climate monitoring and climate science applications.

The ROM SAF also maintains the Radio Occultation Processing Package (ROPP) which contains software modules that aid users wishing to process, quality-control and assimilate radio occultation data from any radio occultation mission into NWP and other models.

The ROM SAF Leading Entity is the Danish Meteorological Institute (DMI), with Cooperating Entities: i) European Centre for Medium-Range Weather Forecasts (ECMWF) in Reading, United Kingdom, ii) Institut D'Estudis Espacials de Catalunya (IEEC) in Barcelona, Spain, and iii) Met Office in Exeter, United Kingdom. To get access to our products or to read more about the ROM SAF please go to: https://www.romsaf.org

Intellectual Property Rights

Abstract

This report briefly discusses the 'anomalous' occultations — those for which the L1 bending angle exceeds the L2 bending angle — that are observed surprisingly often (10–15% of the time) by the GRAS instruments on the Metop satellites. Their distribution in space and time is examined. They are found to be more abundant than average in winter, at night and in a patch in the southern hemisphere. In the first two cases the background electron density is smaller than average; in the third various localised ionospheric features may be at work.

Contents

1 Introduction

Radio occultation measurements are usually made at two different frequencies, typically $f_1 \approx 1.6$ GHz and $f_2 \approx 1.2$ GHz. This is because the ionosphere, through which any radio signal must pass on its way from the GNSS transmitter to the LEO receiver, is dispersive to radio waves at these frequencies. By exploiting this dispersion, observation at two frequencies allows ionospheric effects, which are generally of little interest to NWP users, to be eliminated.

In the simplest case, the refractive index n of air at radio frequency f can be written as (e.g. see [6])

$$n - 1 = k_1 \frac{p_d}{T} + k_2 \frac{e_w}{T} + k_3 \frac{e_w}{T^2} - k_4 \frac{n_e}{f^2}. \tag{1.1}$$

In the above, k_1, k_2, k_3 and k_4 are positive constants, p_d, e_w and T are the dry air pressure, water vapour partial pressure and air temperature, and n_e is the electron density. The first three terms in Eqn (1.1) are independent of frequency. This means that, if the refractivity field is spherically symmetrical, the bending angle at frequency f_i and impact parameter a, $\alpha_i(a)$, is given by the usual Abel integral (e.g. see [9]), and can be written as

$$\alpha_i(a) = A(a) + \frac{B(a)}{f_i^2}, \tag{1.2}$$

where (assuming the refractivity field decreases with height) A is a positive function of a, as is B, provided a is far below the peak of the electron density distribution (e.g. see [4]). Since $f_1 > f_2$, Eqn (1.2) therefore implies that $\alpha_1(a) < \alpha_2(a)$.

It is indeed generally found that the L1 bending angle is less than the L2 one. See, for example, the left hand panel of Fig. 1.1, which shows both bending angles for a typical, 'regular' Metop-A occultation, as well as the 'ionospherically corrected' bending angle, α_{LC}, defined by

$$\alpha_{LC}(a) = \frac{f_1^2 \alpha_1(a) - f_2^2 \alpha_2(a)}{f_1^2 - f_2^2}. \tag{1.3}$$

If Eqn (1.2) is true, then $\alpha_{LC}(a) = A(a)$, the bending angle produced by the neutral atmosphere, because taking the linear combination of $\alpha_1(a)$ and $\alpha_2(a)$ removes the frequency-dependent ionospheric contribution to the bending angle.

More frequently than we might expect, however, the L1 bending angle is found to exceed the L2 bending angle. See, for example, the right hand panel of Fig. 1.1, which shows both bending angles and α_{LC} for an atypical, 'anomalous' Metop-A occultation.

The distribution, abundance and possible explanations of the anomalous occultations observed by the GRAS instruments on the Metop satellites are the subject of this report.

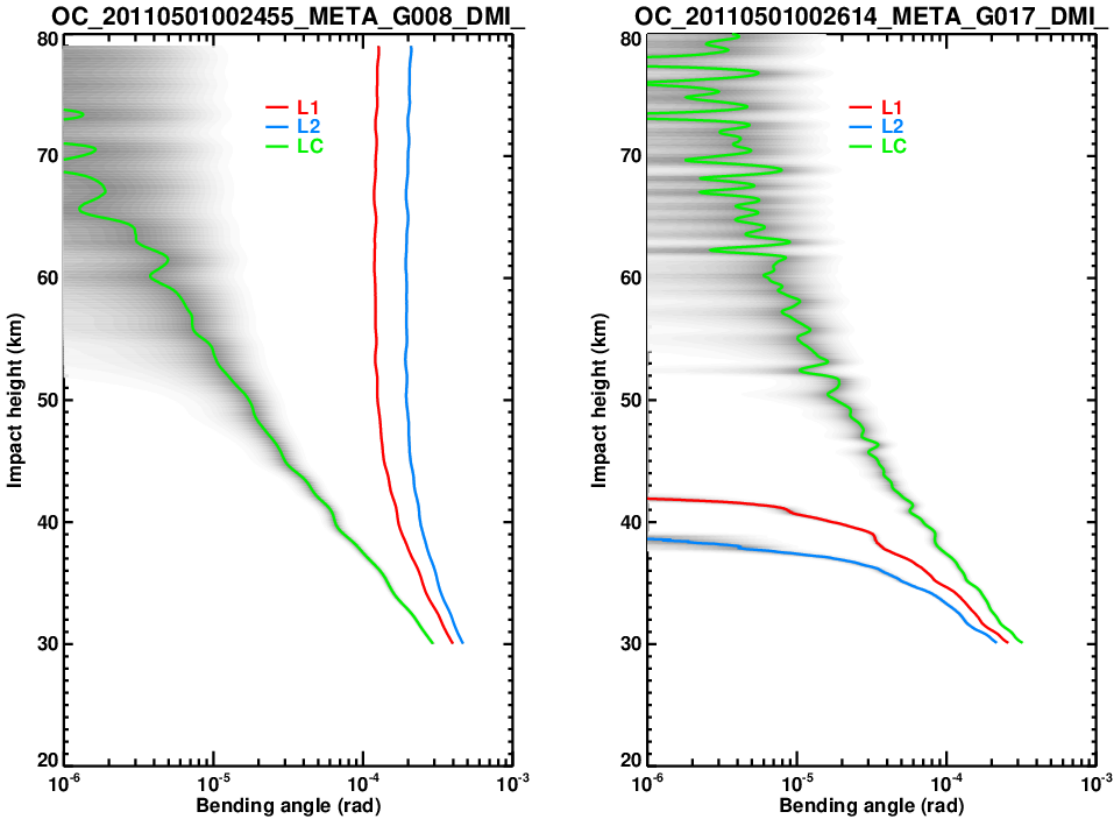

Figure 1.1: Left hand panel: α_{L1}, α_{L2} and α_{LC} for a 'regular' occultation, together with estimates of the uncertainties. Right hand panel: likewise for an 'anomalous' occultation.

2 The evidence

For the purposes of this report, we define an anomalous occultation as one for which the L1 bending angles exceed the L2 bending angles on at least half the impact heights between 49 and 51 km. According to this definition, GRAS instruments on Metop satellites record anomalous occulations 10–15% of the time, and have done so for some time, as can be seen from Fig. 2.1, which shows the global average fraction of anomalous Metop occultations for the past ten years.

Between September 2014 and July 2016 (the grey points in Fig. 2.1), a processor update at EUMETSAT led to a reduction in the number of 'valid' thinned occultations, which are the ones used in this study. Fig. 2.1 shows the fraction of all *observations that are valid and anomalous, which naturally falls when the number of invalid occultations increases. As can be seen, the discrepancy falls away when the PPF change was reverted in August 2016. The grey points in Fig. 2.1 will therefore play no further part in this analysis.*

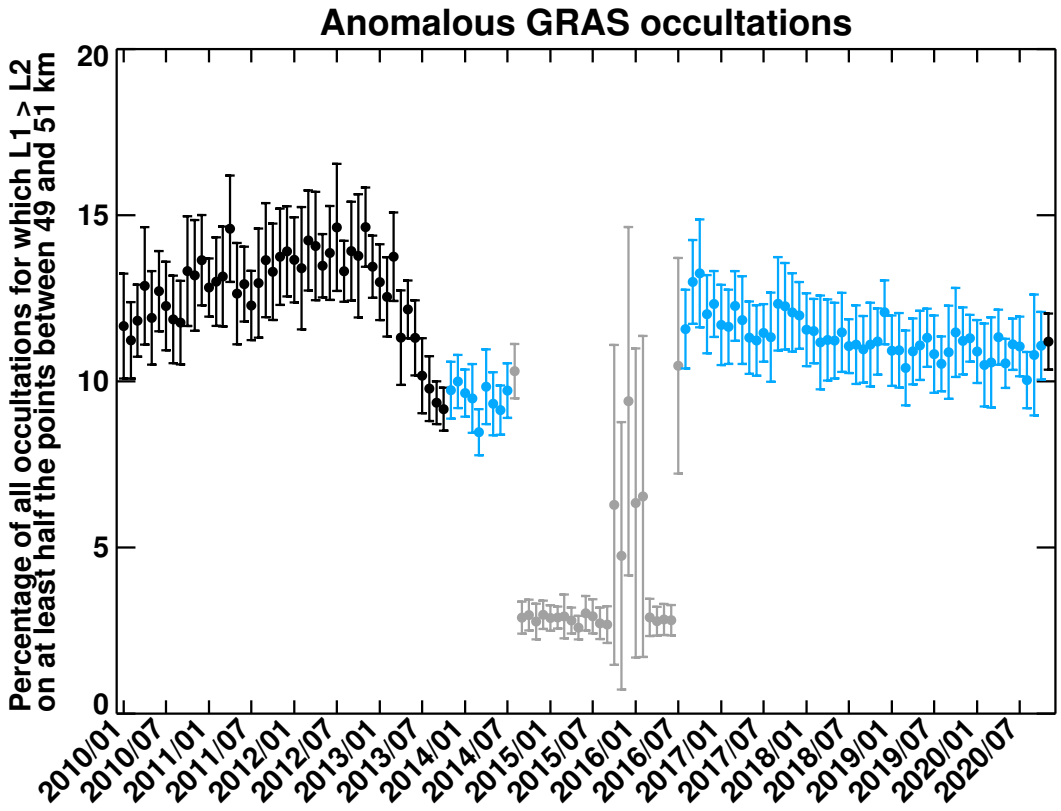

Figure 2.1: Global average fraction of anomalous occultations every month between January 2010 and October 2020.

Ignoring the grey points, then, there is little variation in the mean fraction of anomalous occultations shown in Fig. 2.1, especially after the PPF reset in 2016, when averages to about 12%. Before the PPF change in 2014, there was more variation from year to year, although the average value is about the same. The last solar maximum was in April 2014 (solar cycle 24, [10]), which is when the anomalous occultation rate was at its lowest, but the largest anomalous occultation rate occurs in

2012–13, which does not coincide with the (closest we have to the) last solar minimum in 2009.

The histograms of α_1, α_2, $\alpha_2 - \alpha_1$ (to which the ionospheric components of α_1 and α_2, B/f_1^2 and B/f_2^2, are proportional (see Eqn (1.2)) and α_{LC}, all at 50 km in August 2020, are plotted in Fig. 2.2. They show that both α_1 and α_2 have broad distributions, whose standard deviations are around half of their means. A few percent of both the L1 and L2 bending angles at 50 km are negative. (This is in fact the case for the right hand plot of Fig. 1.1.) Since, according to Eqn (1.2), $\alpha_2 - \alpha_1 = B(a)(f_2^{-2} - f_1^{-2})$, and $f_2 < f_1$, *both ionospheric bending angles $B(a)/f_i^2$ must be negative for anomalous occultations.* Since the atmospheric bending angle decreases roughly exponentially with height, and the ionospheric bending angle is roughly constant, it follows that the total bending will eventually become negative in such cases. The histograms in Fig. 2.2 show that indeed α_{LC} is almost entirely positive, while about 10% of the values of $\alpha_2 - \alpha_1$ are negative. (This matches the anomalous occultation rate for Aug 2020 value in Fig. 2.1.) The standard deviation of $\alpha_2 - \alpha_1$ is less than that of α_1 or α_2, which shows that the L1 and L2 bending angles are positively correlated.

The curious bimodal shapes of the α_1 and α_2 distributions will be explained in Sec. 4.2.

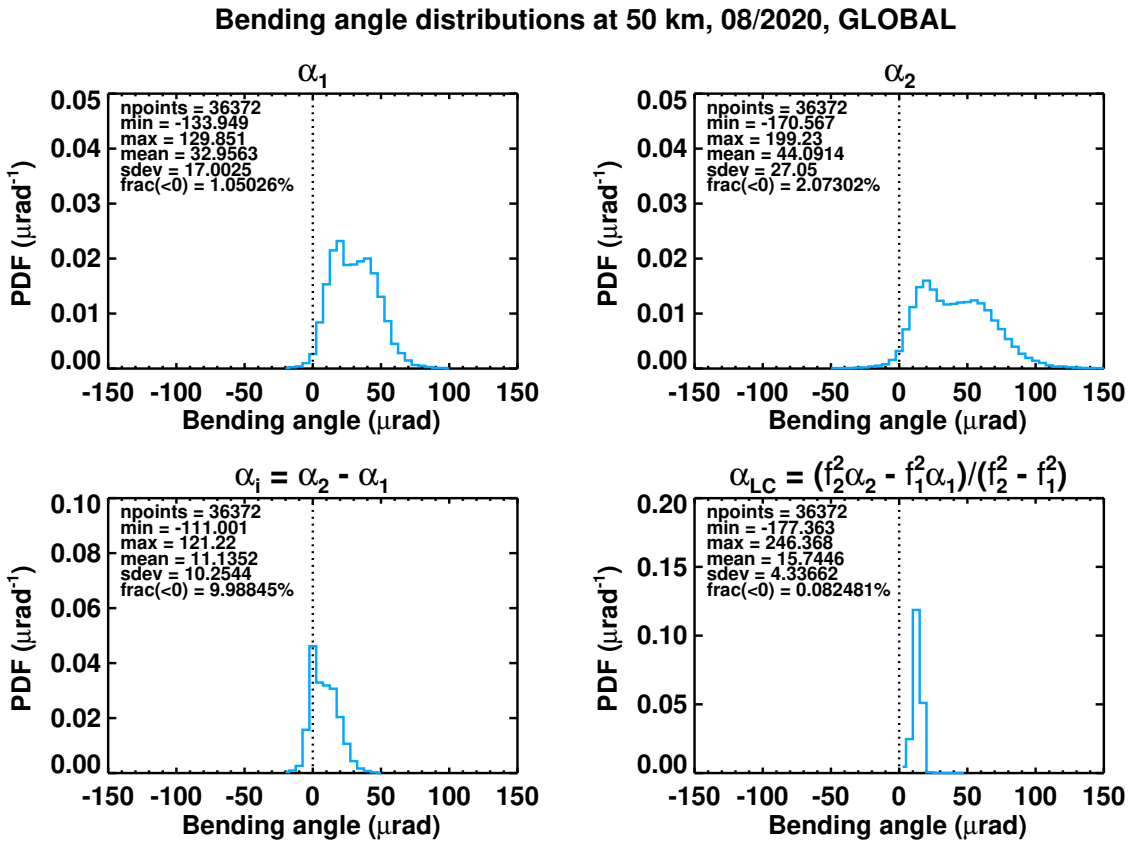

Figure 2.2: Histograms of global bending angles, August 2020.

The global distributions of the occultations in Figs 2.1 and 2.2 hide their variation in space and time. Figs. 2.3 and 2.4 are scatterplots of the regular and anomalous occultations in February and August 2020 respectively. The anomalous occultations are more abundant in the winter hemisphere, although a patch of anomalous occultations persists between about 0–120° E and 50–70° S even in the southern hemisphere summer. This general impression is confirmed by the 2012 timeseries of regular and anomalous occultations in the northern and southern hemispheres, shown in Figs 2.5 and 2.5 respectively. Anomalous occultations are clearly more likely during the winter.

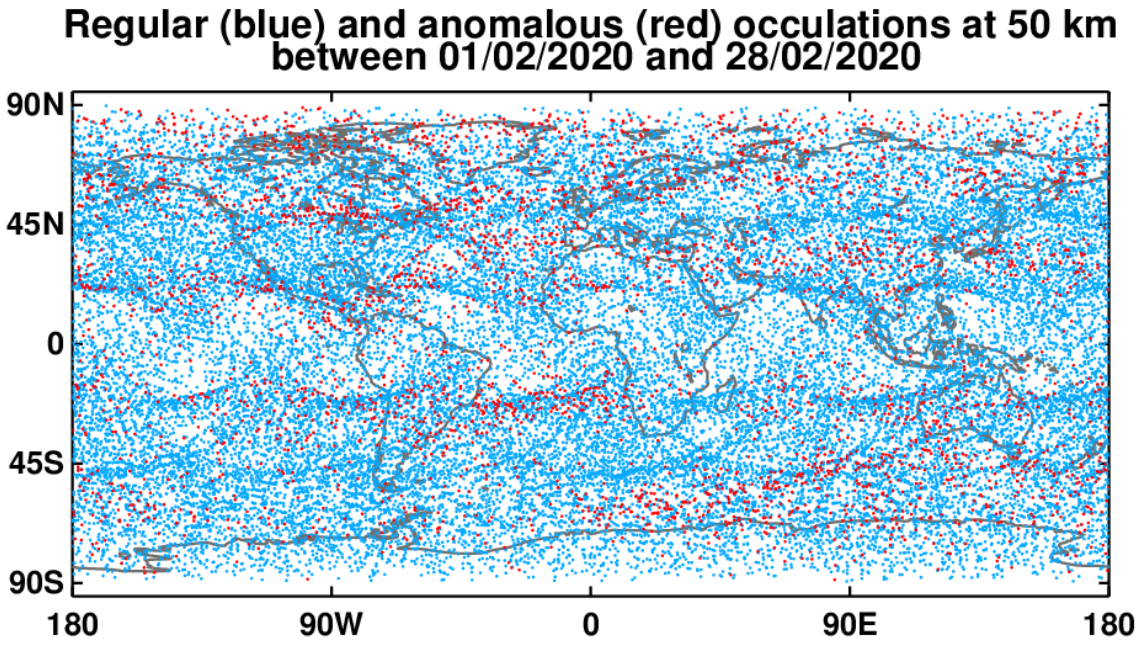

Figure 2.3: Scatterplot of regular and anomalous Metop occultations in February 2020.

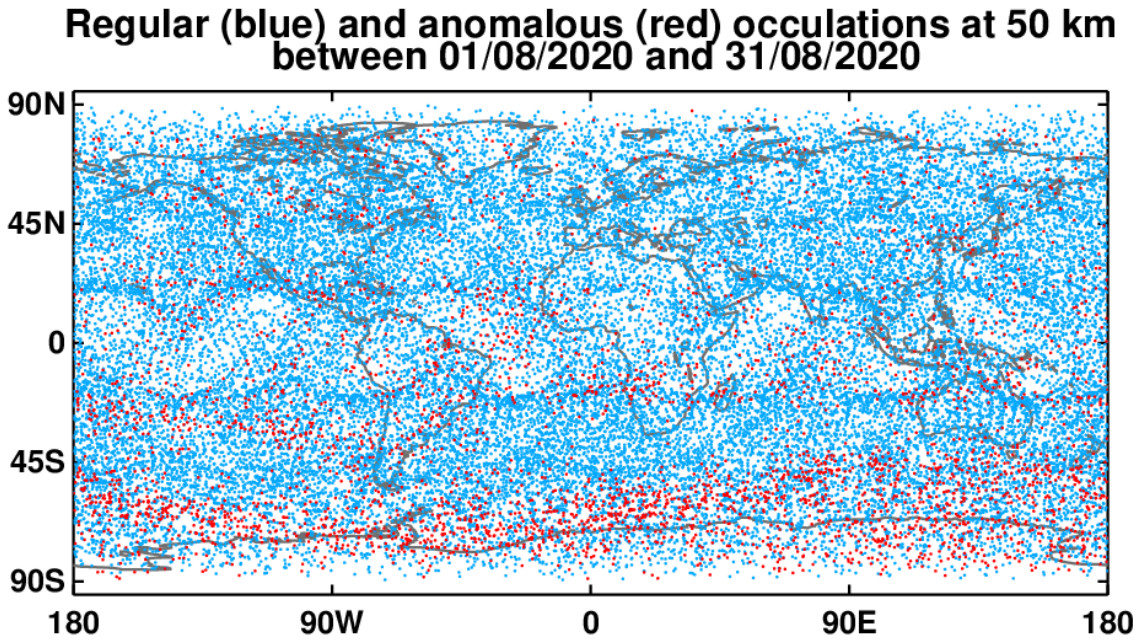

Figure 2.4: Scatterplot of regular and anomalous Metop occultations in August 2020.

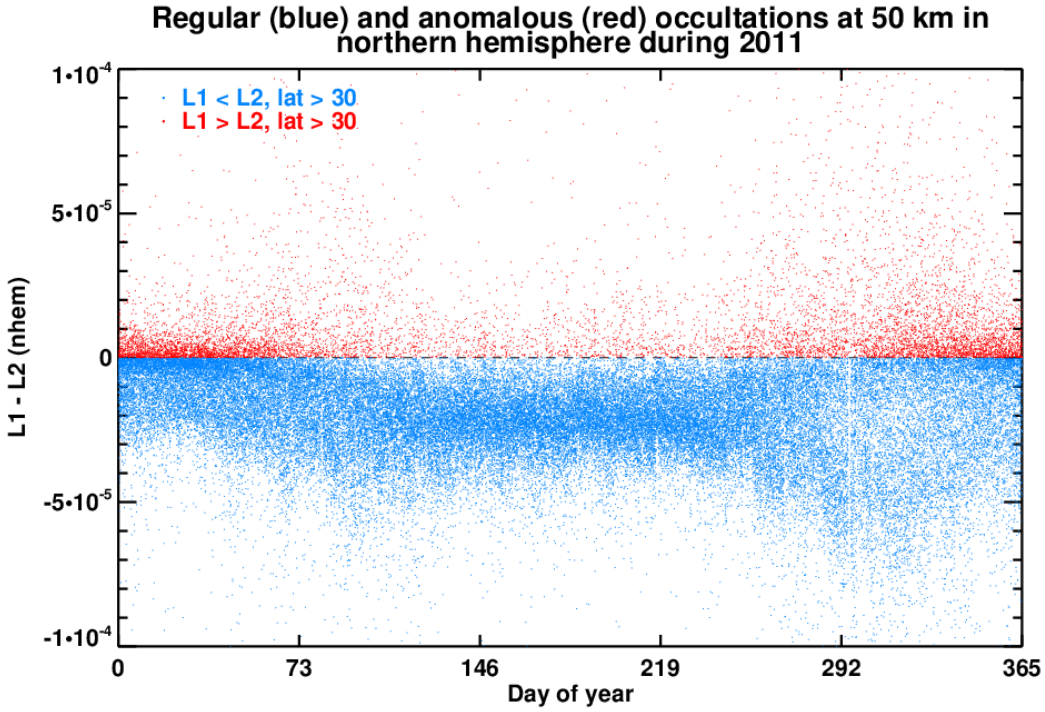

Figure 2.5: Scatterplot of $\alpha_{L1} - \alpha_{L2}$ for northern hemisphere (latitude > 30^o N) Metop occultations during 2011.

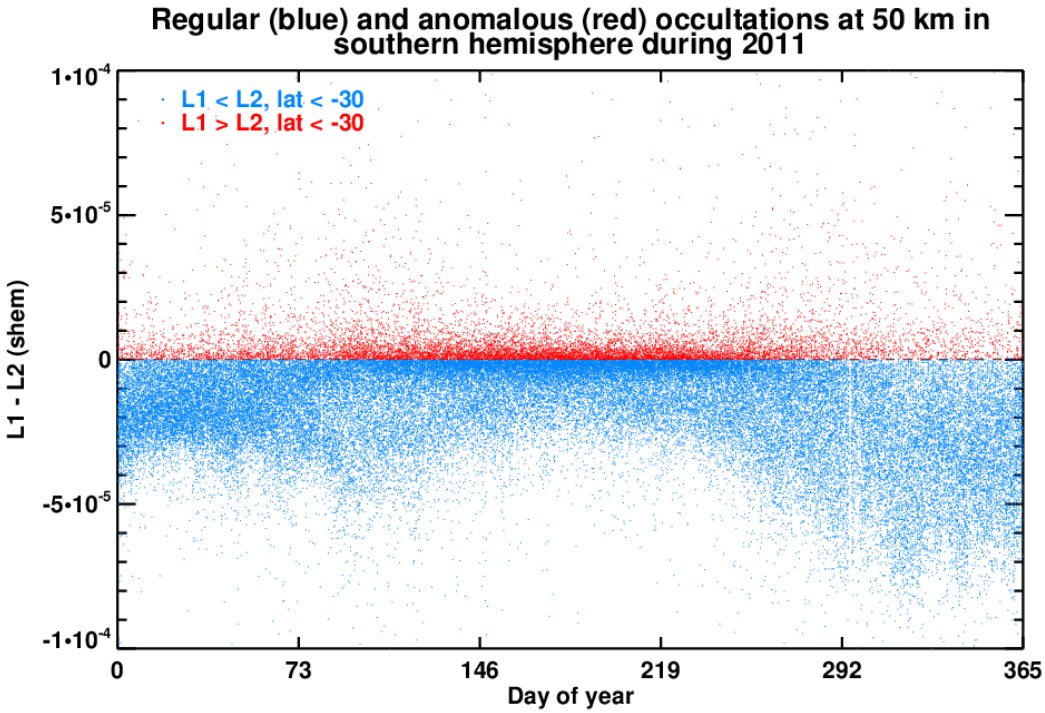

Figure 2.6: Scatterplot of $\alpha_{L1} - \alpha_{L2}$ for southern hemisphere (latitude < 30^o S) Metop occultations during 2011.

There is a diurnal variation, too. Fig. 2.7 shows that the anomalous occultations are more frequent in the night-time, ascending orbit (local time centred around 21:30) than in the daytime, descending orbit (local time centred around 09:30).

It appears, therefore, that anomalous occultations are more frequent when the photo-ionisation that generates the ionospheric electrons is weakest, which is probably when the electron density is smallest.

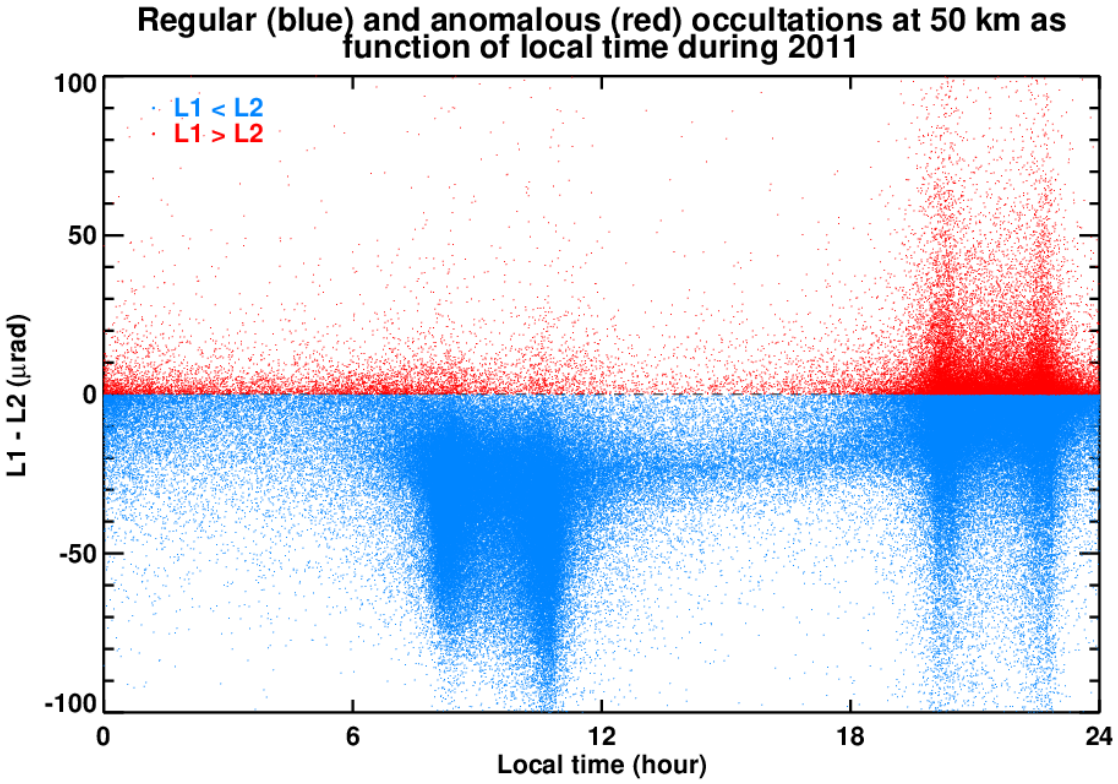

Figure 2.7: Scatterplot of $\alpha_{L1} - \alpha_{L2}$ as a function of local time of Metop occultations during 2011.

3 Further analysis

L1 and L2 bending angles at 50 km from Metop occultations for the 60 months between November 2013 and July 2014 inclusive, and August 2016 and October 2020 inclusive — that is, the blue points in Fig. 2.1 — have been aggregated onto a 10° by 10° global grid. Data from the five Januarys in the timeseries have been averaged into a mean January, and likewise for the other months. The fraction of anomalous occultations at any time t in the resulting timeseries, $f(t)$, is Fourier decomposed as

$$f(t) = c_0 + c_1 \cos(\omega t - \phi_1) + c_2 \cos(2\omega t - \phi_2) + \ldots, \tag{3.1}$$

where $\omega = 2\pi/(12 \text{ months})$, c_0 is the time-mean of $f(t)$, $c_i(>0)$ for $i = 1,2,\ldots$ is the amplitide of the i^{th} mode and ϕ_i is its phase offset (between $-\pi$ and π). f, c_i and ϕ_i all depend on location.

Maps of c_0 and c_1 are shown in Figs. 3.1 and 3.2 respectively. The mean fraction of anomalous occultations, shown in Fig. 3.1, is about 11%, as expected from Fig. 2.1. They are, however, more abundant poleward of about 50° S, and especially in a patch centred around (30° E, 60° S), where they occur in almost 30% of all occultations. The amplitude of the annual cycle of anomalous occultations, shown in Fig. 3.2, peaks in the extratropics, which strengthens the suggestion of a bias in favour of the winter hemisphere. There is again a higher amplitude in the southern hemisphere, peaking this time in a patch centred around 70° W, 75° S). There is less annual variation in the 'hot spot' of Fig. 3.1, suggesting that this is a more permanent feature. This is confirmed by Fig. 3.4, which shows the timeseries of anomalous occulations in the regions marked '1' in Fig. 3.1 and '2' in Fig. 3.2. Region 1 has a small annual variation about its mean; in region 2 the amplitude of the annual cycle is comparable to the time-averaged value.

The phase offset of the annual cycle, ϕ_1, is shown in Fig. 3.3. It clearly shows that the northern hemisphere extratropical annual cycle peaks in January ($\phi_1 \approx 0$), in contrast to the southern hemisphere extratropical annual cycle, which peaks in July ($\phi_1 \approx \pi$). The latter feature is also apparent from Fig. 3.4. The picture in the tropics is a confusing mixture of both, but Fig. 3.2 shows that the amplitude is small there anyway. (Phases of π and $-\pi$ are equivalent in Eqn (3.1), but they average to 0, to which they are not equivalent, so the zonal means in this figure have been calculated as the principal value of the argument of the zonal mean of $\exp(i\phi_1)$.)

Maps of c_2, c_3 and c_4 (not shown) do not display any suggestive geographical features, and are typically about three times smaller than c_1 anyway. c_1 accounts for about 61% of the variance of the full timeseries; c_2, c_3 and c_4 add about 6% to this total. The rest of the variance appears to be small scale noise concentrated around the poles.

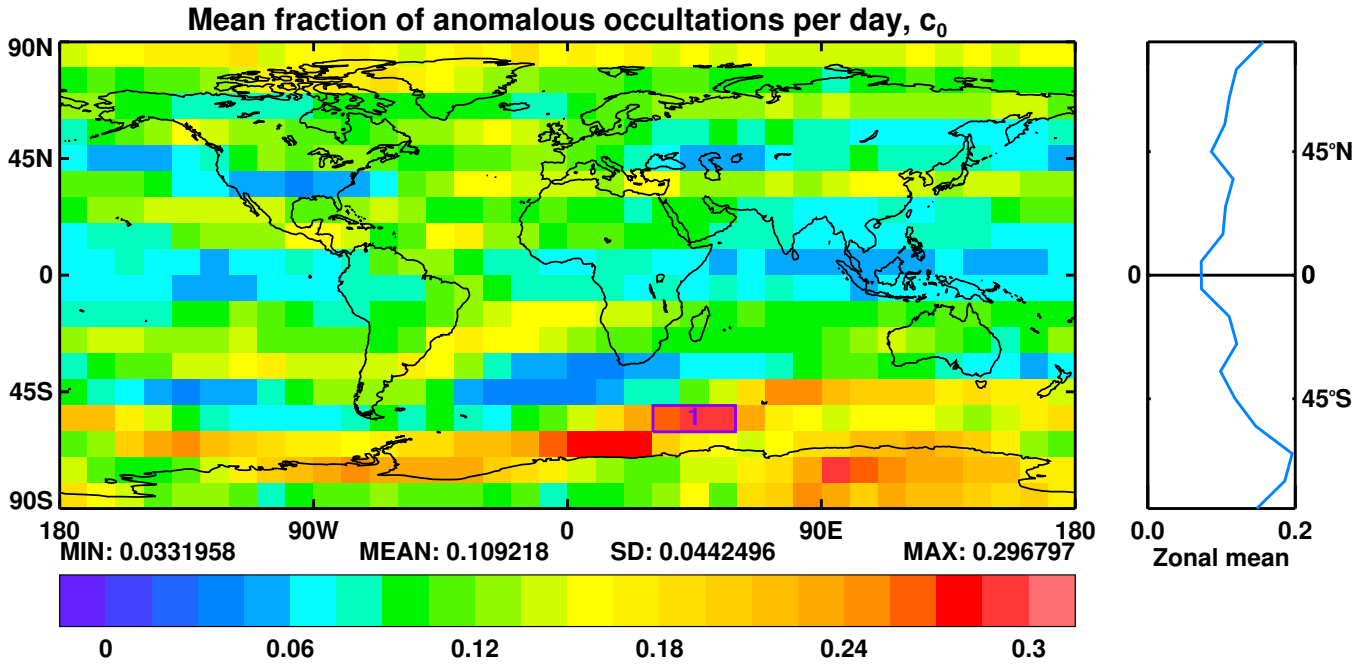

Figure 3.1: Map of c_0 in Eqn (3.1). Data from [11/2013, 7/2014] ⋃ [8/2016, 10/2020]

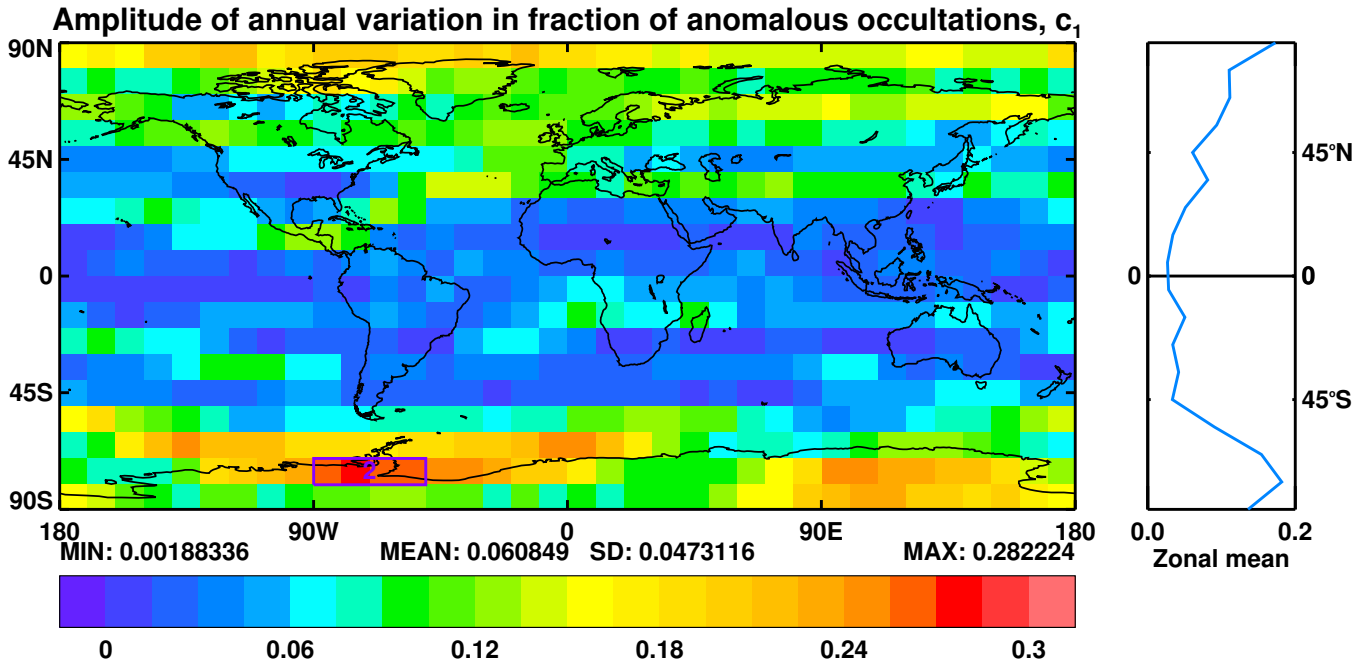

Figure 3.2: Map of c_1 in Eqn (3.1). Data from [11/2013, 7/2014] ⋃ [8/2016, 10/2020]

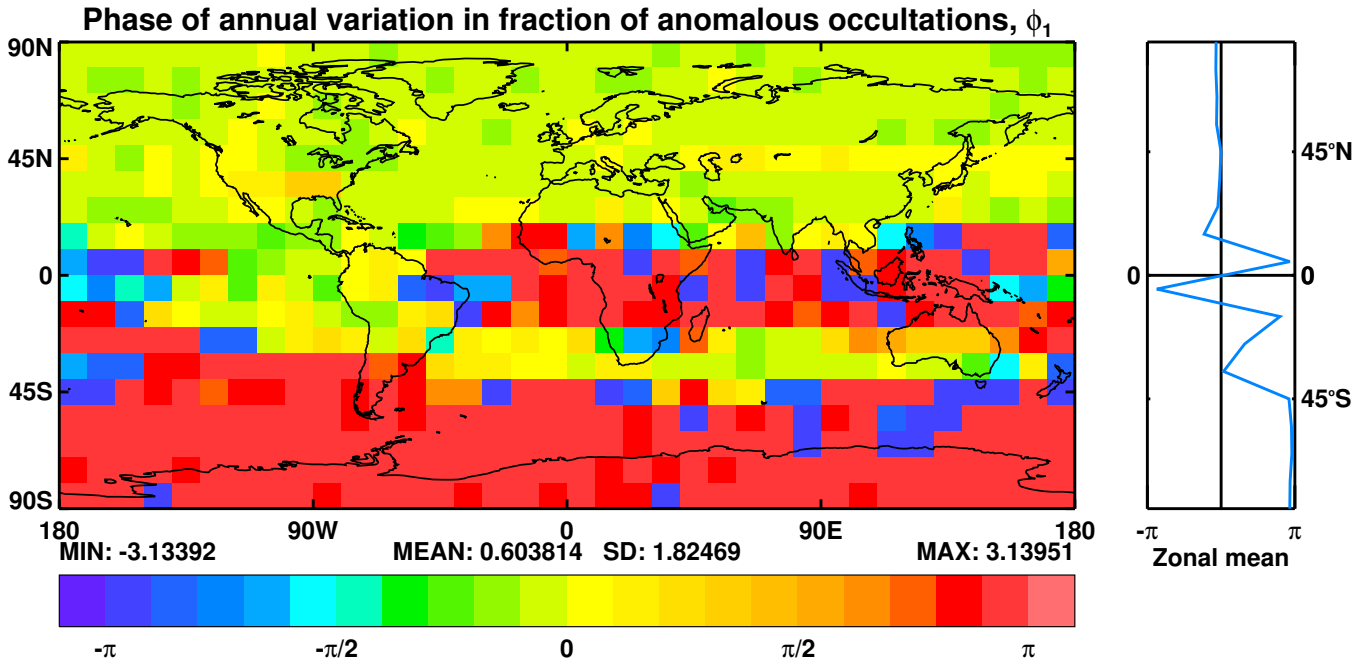

Figure 3.3: Map of ϕ_1 in Eqn (3.1). Data from [11/2013, 7/2014] $\cup$ [8/2016, 10/2020]

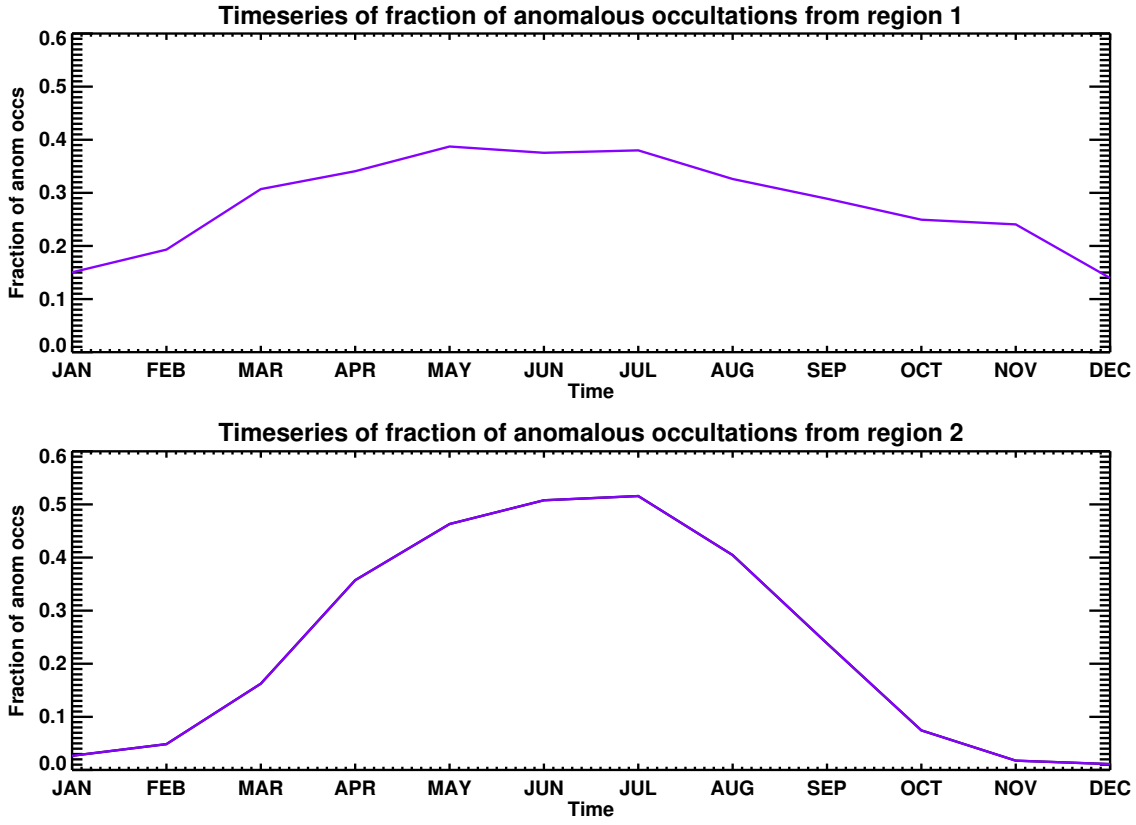

Figure 3.4: Timeseries of anomalous occulation fractions over region 1 in Fig. 3.1 and region 2 in Fig. 3.2.

4 Discussion

We have seen that, overall, anomalous occulations occur about 10–15% of the time for the GRAS receiver on the Metop satellites. There is strong evidence that they occur more often at night and in winter. These will be reduced photo-ionisation at these times, and therefore it is natural to suppose that anomalous occultations are favoured when the electron density in the ionosphere is small. This is when the ionospheric bending itself is small. Several more aspects will now be briefly discussed.

4.1 Absence of spherical symmetry

Spherical symmetry is used to deduce Eqn (1.2), which is the reason for supposing that the L2 bending angle should be greater than the L1 bending angle. In a simple slab model ionosphere, Culverwell and Healy ([4]) estimated the size of the constant horizontal electron density gradient that would be needed to reverse this inequality, by nullifying the intrinsically positive bending. They found that the electron density would need to change by around 40% over the $\sim$350 km[1] of the ionosphere that the ray passes through on its entry to and exit from the neutral atmosphere. These gradients would need to appear in both passages of the ray through the ionosphere, to prevent the overall bending from still being positive. Although gradients of this magnitude can certainly arise, it seems unlikely that they occur often enough to explain the observed frequency ($\sim$10–15%) of anomalous occultations.

4.2 Statistical noise

Fig. 2.2 shows that the probability distributions of the L1 and L2 bending angles are rather broad. In the region where they overlap, the L1 bending angles exceed the L2 ones, and the degree of that overlap might be expected to increase as the ionospheric component of the bending decreases, and α_1 and α_2 converge, provided that the width of the distributions does not decrease in a compensating way. Evidence in support of this is provided by Figs 4.1 and 4.2, which separates the distribution of bending angles at 50 km in August 2020, as shown in Fig. 2.2, into the extratropical northern hemisphere (latitude > 30^o N) and southern hemisphere (latitude < 30^o S) parts. In the summer (northern) hemisphere, where the background electron density and ionospheric bending are relatively large, α_1 and α_2 have large mean values, and the mean of $(\alpha_2 - \alpha_1)$ is about 14 μrad. The standard deviation of $(\alpha_2 - \alpha_1)$ is around 8 μrad, and about 3% of the occultations are anomalous. In the winter (southern) hemisphere, however, where the background electron density and ionospheric bending are smaller, α_1 and α_2 have much smaller mean values, and the mean value of $(\alpha_2 - \alpha_1)$ is about 5 μrad. The standard deviations of α_1 and α_2 are about the same, however, as is that of $\alpha_2 - \alpha_1$, which remains around 7–8 μrad. This means that about 18% of the southern hemisphere occultations are anomalous.

The difference between the summer and winter bending angle distributions in Figs 4.1 and 4.2 is clear. By combining the α_1 and α_2 distributions by eye, the reader will be able to see how the bimodal distributions shown in the global data in Fig. 2.2 arise.

[1] Not the 670 km wrongly estimated in RSR 17.

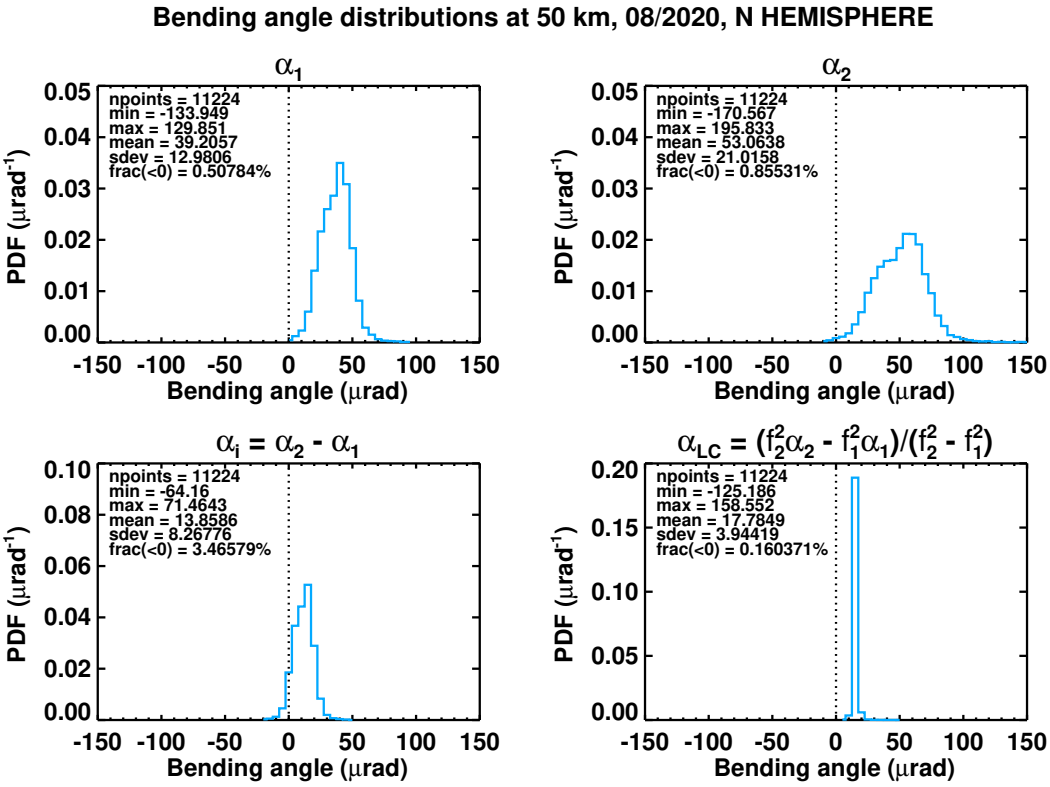

Figure 4.1: Histograms of extratropical northern hemisphere bending angles, Aug. 2020.

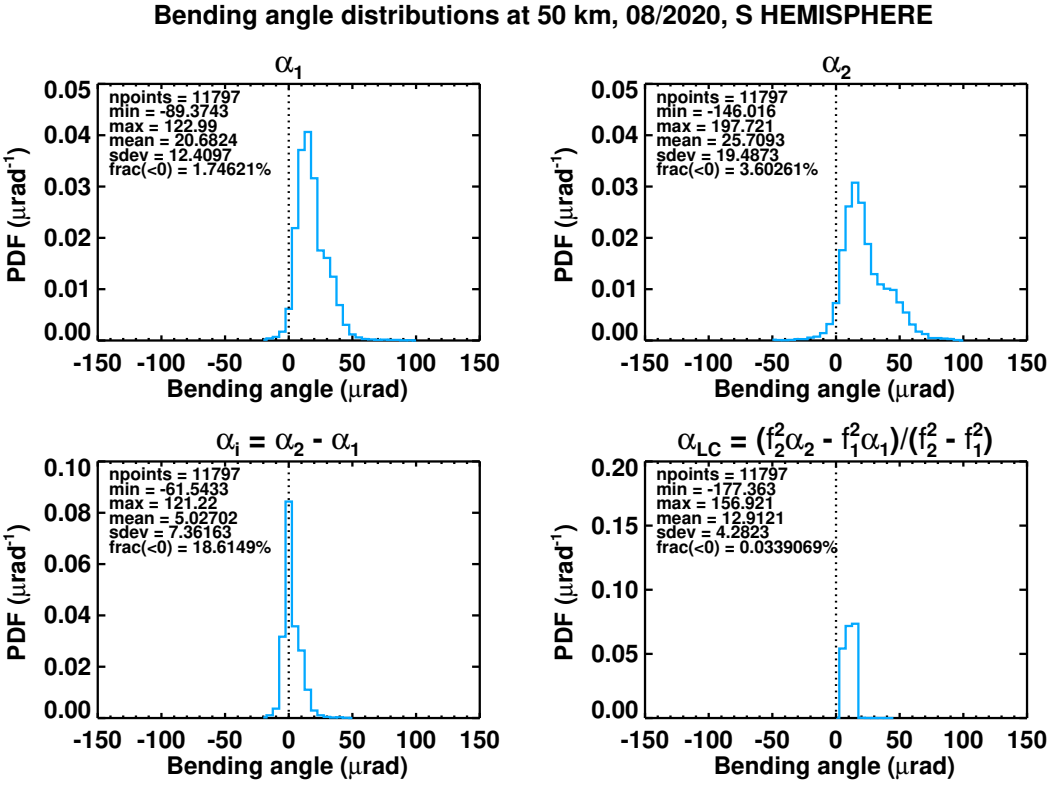

Figure 4.2: Histograms of extratropical southern hemisphere bending angles, Aug. 2020.

4.3 Effects of electron density at LEO

The bending angles in this study have been calculated by assuming that the electron density, and therefore the refractivity, is zero at the Metop satellite. This is not strictly true, and although the effects are small, they are systematic, since the LEO electron density is never negative.

In [5], Healy shows that, to account for the mis-specified refractive index at the LEO, the observed bending angles at a given impact parameter a must be *increased* by

$$\Delta\alpha_i(a) = \frac{k_4}{f_i^2}\frac{a}{\sqrt{r(\mathrm{LEO})^2 - a^2}} n_e(\mathrm{LEO}). \tag{4.1}$$

The zonal mean TEC (vertically integrated electron density) is around 25 TECU in the tropics and 15 TECU in the extratropics ([4]). (1 TECU = 10^{16} electrons/m^2.) For an ionospheric F-layer of strength 20 TECU, centred at 300 km and having a width of 75 km, the correction in Eqn. (4.1) amounts to about 1.0 μrad for α_1 and 1.6 μrad for α_2 at 50 km (although in fact there is little variation with height, up to 80 km at least). $\alpha_2 - \alpha_1$ must therefore be increased by about 0.6 μrad. This is in the right direction, but a glance at the $\alpha_2 - \alpha_1$ distribution in Fig. 2.2 shows that it is probably not large enough to reduce significantly the number of anomalous occultations — especially when it is realised that the correction increases with LEO electron density, whereas we have seen plenty of evidence that anomalous occultations are more abundant when the electron density is low. In fact, a small side calculation, simply adding 1.0 μrad to α_1 and 1.6 μrad to α_2, reduces the fraction of anomalous occultations in August 2020 from 10% (Fig. 2.2) to 8% (not shown). But the fraction of anomalous occultations, in the sharply decreasing tail of the $\alpha_2 - \alpha_1$ distribution, is strongly dependent on the position of the centre of that distribution, which depends on the TEC and the peak height and width of the $n_e(r)$ profile. Variations from the above average values of these parameters might lead to significant numbers of anomalous occultations. The idea should not be abandoned yet.

4.4 Geographical distribution

The persistent patch of anomalous occultations in the southern hemisphere, as shown in Fig. 3.1, is curious. It may be related to the South Atlantic Anomaly (SAA), the area where the inner Van Allen radiation belt dips closest to the surface of the earth (e.g. [7]). But the SAA is centred further west, at around 40^o W, and in any case it is not clear that it would affect the background electron density in a way that explains the distribution of the anomalous occultations.

Another possible explanation is that anomalous occultations are more common in ionospheric troughs, which are circumpolar regions of the ionospheric F-layer where the night-time electron density is anomalously low (e.g. [8]). The electron density gradients in these troughs are certainly strong enough to reverse the intrinsically positive bending. (The schematic figure in [8] suggests electron density changes of over 300% in 350 km.) And the strong diurnal variation is shared by the anomalous occultations. On the other hand, there are mid-latitude ionospheric troughs in both hemispheres, and Fig. 3.1 shows a clear north-south asymmetry in the pattern of the anomalous occultations. And again, it is not clear that troughs occur frequently enough to explain the $\sim$30% anomalous occultation rate over the Southern Indian Ocean.

Finally, it has been suggested that polar holes — night-time depletions of the ionospheric F-layer, poleward of about 70^o N or S (e.g. [1]) — may help to explain the geographical distribution of the anomalous occultations. Polar holes have strong electron density gradients at their edges, and we have noted that these could generate negative bending angles and therefore anomalous occultations. There are, however, polar holes over the Arctic as well as the Antarctic. In addition, the anomalous

occultations have persisted at a steady rate for at least 10 years (see Fig. 2.1), whereas ionospheric polar holes are rather active features, changing location and intensity on an hourly timescale ([2]). There would need to be enough of them to produce a steady average if polar holes were to play a significant part in the story of the anomalous occultations.

5 Conclusions and outlook

This report has briefly discussed the 'anomalous' occultations — those for which the L1 bending angle exceeds the L2 bending angle — that are observed surprisingly often (10–15% of the time) by the GRAS instruments on the Metop satellites. Their distribution in space and time has been examined. They have been shown to be more abundant than average in winter, at night and in a patch in the southern hemisphere. In the first two cases the background electron density is smaller than usual, in the third various localised ionospheric features may be at work.

Various explanations have been briefly discussed. The presence of horizontal electron density gradients is an obvious explanation, since spherical symmetry implies strongly that the L2 bending angle should exceed the L1 one. It is, however, difficult to see how electron density gradients, strong enough to reverse the natural tendency towards positive bending angles, could arise frequently enough to explain the observed 10–15% abundance of anomalous occultations. The statistical distributions of the L1 and L2 bending angles are broad enough that they overlap, so that as the electron density falls and the two distributions converge, the degree of overlap increases and thus we observe more occultations with α_1 exceeding α_2. But this does not explain why we find negative ionospheric bending angles in the first place. Failure to account for the finite electron density at the Metop satellites might explain it, but correcting this oversight does not, in the simplest analysis, eliminate many of the anomalous occultations. But the abundance of these is sensitive to the details of the electron density distribution. It could be rewarding to repeat the analysis if reliable estimates of this distribution became available.

The practical importance of anomalous occultations in operational weather forecasting remains unclear. Are they symptomatic of a fundamental bending angle observation problem, meaning that they should be rejected from the assimilation process, or is the cause of the anomalous behaviour successfully removed by the usual linear combination of the L1 and L2 bending angles, leaving behind useful neutral atmosphere information? (Any effects arising from the finite electron density at the LEO *would* be absent from α_{LC}.) An NWP trial that tested the impact of removing the anomalous occultations from the operational assimilation system should answer this question.

Finally, attempts have recently been made to retrieve ionospheric electron density profiles by using measurements of the difference between the L2 and L1 bending angles (e.g. [3]). As we have seen, anomalous occultations imply negative electron densities if spherical symmetry is assumed. They would therefore need to be screened out of any programme to assimilate such data using a spherically symmetric forward model. On the other hand, such retrievals may shed light on the cause of these curious occultations.

Acknowledgements

We are indebted to Axel von Engeln of EUMETSAT for providing the 2011 Metop L1 and L2 bending angles at 50 km. Edmund Henley (Met Office) provided much useful information and advice regarding the ionospheric aspects of this work. We also thank Sean Healy of ECMWF for useful discussions throughout the work.

This work was carried out as part of EUMETSAT's Radio Occultation Meteorology Satellite Application Facility (ROM SAF) which is a decentralised operational RO processing centre under EUMETSAT.

Bibliography

[1] H. C. Brinton, J. M. Grebowsky and L. H. Brace, The high-latitude winter F region at 300 km: thermal plasma observations from AE-C, J. Geop. Res., Vol. 83, A10, 4767–4776, 1978.

[2] G. Crowley, H. C. Carlson, S. Basu, W. F. Denig, J. Buchau, and B. W. Reinisch, The dynamic ionospheric polar hole, Radio Science, Vol. 28, No. 3, 401–413, 1993.

[3] H. Lyu, M. Hernández-Pajares, E. Monte-Moreno and E. Cardellach, Electron density retrieval from truncated radio occultation GNSS data, Journal of Geophysical Research: Space Physics, 124, 4842–4851, doi.org/10.1029/2019JA026744, 2019.

[4] I. D. Culverwell and S. B. Healy, Simulation of L1 and L2 bending angles with a model ionosphere, SAF/ROM/METO/REP/RSR/017, 2015.

[5] S. B. Healy, Some science changes in ROPP-9.1, SAF/ROM/METO/REP/RSR/033, 2018.

[6] E. G. Kursinski, J. Hajj, J. Schofield, R. Linfield and K. Hardy, Observing earth's atmosphere with radio occultation measurements using the Global Positioning System, J. Geophys. Res., 102, 23.429–23.465, 1997.

[7] NASA Goddard Space Flight Center, South Atlantic Anomaly, https://heasarc.gsfc.nasa.gov/docs/rosat/gallery/misc_saad.html

[8] A. S. Rodger and M. Pinnock, Movements of the mid-latitude ionospheric trough, J. Atmos. and Terr. Phys., Vol. 44, No. 11, 985–492. 1982.

[9] C. D. Rodgers, Inverse Methods for Atmospheric Sounding - Theory and Practice, World Scientific, 2000.

[10] Space Weather Prediction Center, Solar Cycle 25 Forecast Update, https://www.swpc.noaa.gov/news/solar-cycle-25-forecast-update

ROM SAF (and earlier GRAS SAF) Reports

SAF/GRAS/METO/REP/GSR/001	Mono-dimensional thinning for GPS Radio Occulation
SAF/GRAS/METO/REP/GSR/002	Geodesy calculations in ROPP
SAF/GRAS/METO/REP/GSR/003	ROPP minimiser - minROPP
SAF/GRAS/METO/REP/GSR/004	Error function calculation in ROPP
SAF/GRAS/METO/REP/GSR/005	Refractivity calculations in ROPP
SAF/GRAS/METO/REP/GSR/006	Levenberg-Marquardt minimisation in ROPP
SAF/GRAS/METO/REP/GSR/007	Abel integral calculations in ROPP
SAF/GRAS/METO/REP/GSR/008	ROPP thinner algorithm
SAF/GRAS/METO/REP/GSR/009	Refractivity coefficients used in the assimilation of GPS radio occultation measurements
SAF/GRAS/METO/REP/GSR/010	Latitudinal Binning and Area-Weighted Averaging of Irregularly Distributed Radio Occultation Data
SAF/GRAS/METO/REP/GSR/011	ROPP 1dVar validation
SAF/GRAS/METO/REP/GSR/012	Assimilation of Global Positioning System Radio Occultation Data in the ECMWF ERA-Interim Re-analysis
SAF/GRAS/METO/REP/GSR/013	ROPP PP validation
SAF/ROM/METO/REP/RSR/014	A review of the geodesy calculations in ROPP
SAF/ROM/METO/REP/RSR/015	Improvements to the ROPP refractivity and bending angle operators
SAF/ROM/METO/REP/RSR/016	Simplifying EGM96 undulation calculations in ROPP
SAF/ROM/METO/REP/RSR/017	Simulation of L1 and L2 bending angles with a model ionosphere
SAF/ROM/METO/REP/RSR/018	Single Frequency Radio Occultation Retrievals: Impact on Numerical Weather Prediction
SAF/ROM/METO/REP/RSR/019	Implementation of the ROPP two-dimensional bending angle observation operator in an NWP system
SAF/ROM/METO/REP/RSR/020	Interpolation artefact in ECMWF monthly standard deviation plots
SAF/ROM/METO/REP/RSR/021	5th ROM SAF User Workshop on Applications of GPS radio occultation measurements
SAF/ROM/METO/REP/RSR/022	The use of the GPS radio occultation reflection flag for NWP applications
SAF/ROM/METO/REP/RSR/023	Assessment of a potential reflection flag product
SAF/ROM/METO/REP/RSR/024	The calculation of planetary boundary layer heights in ROPP
SAF/ROM/METO/REP/RSR/025	Survey on user requirements for potential ionospheric products from EPS-SG radio occultation measurements

ROM SAF (and earlier GRAS SAF) Reports (cont.)

SAF/ROM/METO/REP/RSR/026	Estimates of GNSS radio occultation bending angle and refractivity error statistics
SAF/ROM/METO/REP/RSR/027	Recent forecast impact experiments with GPS radio occultation measurements
SAF/ROM/METO/REP/RSR/028	Description of wave optics modelling in ROPP-9 and suggested improvements for ROPP-9.1
SAF/ROM/METO/REP/RSR/029	Testing reprocessed GPS radio occultation datasets in a reanalysis system
SAF/ROM/METO/REP/RSR/030	A first look at the feasibility of assimilating single and dual frequency bending angles
SAF/ROM/METO/REP/RSR/031	Sensitivity of some RO measurements to the shape of the ionospheric electron density profile
SAF/ROM/METO/REP/RSR/032	An initial assessment of the quality of RO data from KOMPSAT-5
SAF/ROM/METO/REP/RSR/033	Some science changes in ROPP-9.1
SAF/ROM/METO/REP/RSR/034	An initial assessment of the quality of RO data from Metop-C
SAF/ROM/METO/REP/RSR/035	An initial assessment of the quality of RO data from FY-3D
SAF/ROM/METO/REP/RSR/036	An initial assessment of the quality of RO data from PAZ
SAF/ROM/METO/REP/RSR/037	6th ROM SAF User Workshop
SAF/ROM/METO/REP/RSR/038	An initial assessment of the quality of RO data from COSMIC-2
SAF/ROM/METO/REP/RSR/039	Impacts of RO mission differences on trends in multi-mission data records

ROM SAF Reports are accessible via the ROM SAF website: http://www.romsaf.org